Creep properties and precipitate evolution in Al–Li alloys microalloyed with Sc and Yb

Matthew E. Krug [a],[1], David N. Seidman [a],[b], David C. Dunand [a],*

[a] Department of Materials Science and Engineering, Northwestern University, 2220 Campus Drive, Evanston, IL 60208, USA
[b] Northwestern Center for Atom Probe Tomography, Northwestern University, 2220 Campus Drive, Evanston, IL 60208, USA

ABSTRACT

A dilute Al–Sc alloy (Al–0.12 Sc, at.%, Al–Sc), its counterpart with a Li addition (Al–2.9 Li–0.11 Sc, at.%, Al–Li–Sc), as well as a quaternary alloy (Al–5.53 Li–0.048 Sc–0.009 Yb, at.%, Al–Li–Sc–Yb) were isothermally aged at 325 °C, and in some cases isochronally aged to 450 °C. As the α'-Al$_3$(Li,Sc) and Al$_3$(Li,Sc,Yb) precipitates, with L1$_2$ structure, coarsen in the two Li-containing alloys, their Li and Yb concentrations decrease and their Sc concentration increases. A significant interfacial excess of Li also segregates at the α-Al matrix/α'-Al$_3$Sc(Li,Sc,Yb) precipitate interface: 5.99 ± 0.05 atoms nm^{-2} in Al–Li–Sc and 13.2 ± 0.4 atoms nm^{-2} in Al–Li–Sc–Yb after aging isochronally to 450 °C. During compression creep at 300 °C, the aged alloys exhibit threshold stresses between 8 and 22 MPa. A recent threshold stress model based on elastic interactions between dislocations and precipitates predicts correctly that Li additions in the Al–Li–Sc alloy reduce the threshold stress, while Yb in the Al–Li–Sc–Yb alloy increases it. The model is also in agreement with the threshold stresses of all Al–Sc–X alloys published to date.

© 2012 Elsevier B.V. All rights reserved.

1. Introduction

Dilute Al–Sc alloys exhibit excellent creep resistance at elevated temperatures [1–3], due to the presence of nanoscale L1$_2$-ordered α'-Al$_3$Sc precipitates that are coarsening-resistant to ~300 °C [1–5]. The α'-Al$_3$Sc(L1$_2$) phase precipitates during aging of supersaturated Al–Sc below the maximum solid solubility of Sc in Al of 0.23 Sc (all compositions are given in at.%) at 660 °C [6]); they are coherent, and have an unconstrained lattice parameter mismatch with the α-Al(f.c.c.) matrix of 1.33% at ambient temperature and 1.07% at 300 °C [7]. Relative to pure Al, the presence of α'-Al$_3$Sc(L1$_2$) precipitates improves the creep resistance of coarse-grained Al–Sc alloys by inhibiting dislocation motion, leading to a threshold stress below which the deformation rate becomes too small for practical laboratory measurement [8–10].

The effects of ternary alloying additions on the α'-Al$_3$Sc(L1$_2$) precipitate structure and the mechanical properties of Al–Sc alloys have been studied in detail. On isothermal aging at 300 °C, additions of rare earth (RE) elements (Dy, Er, Gd, Sm, Y, and Yb [11] as well as Tb, Ho, Tm and Lu [12]) to binary Al–Sc alloys result in core/shell

α'-Al$_3$(Sc$_{1-x}$RE$_x$) precipitates with a RE-rich core within a Sc-rich shell. Rare-earth elements substitute for Sc on its sublattice in the L1$_2$ structure, resulting in an increase in the lattice parameter mismatch with the α-Al matrix [13,14]. Because the threshold stress in these alloys is due to elastic interactions between the misfitting precipitates and the matrix [15,16], RE additions to a binary Al–Sc alloy improve its creep resistance [17,18], while also decreasing its cost [19] due to the replacement of up to 30% of the more expensive Sc [12]. The effect of additions of the transition metals (TM) Ti and Zr to Al–Sc on creep resistance was also studied [20–24]. These elements decrease the lattice parameter mismatch of the precipitates [14], and hence the creep resistance is decreased [20–24]. Finally, the effect of Mg-additions on creep of Al–Sc was investigated [25]. Although Mg has only negligible solubility in α'-Al$_3$Sc(L1$_2$) [26], Mg has a large solid solubility in α-Al, resulting in an increase in the lattice parameter of Al(Mg) relative to pure Al, and therefore a decrease in the lattice parameter mismatch with α'-Al$_3$Sc. The effect is, however, small, and therefore the creep behavior is not significantly degraded [25].

Lithium is a unique addition to binary Al–Sc alloys, because like Mg it has a large solubility in α-Al (13.1 at.% at the eutectic temperature, 603 °C [27]), and similar to the TM and RE elements, it has significant solubility in α'-Al$_3$Sc, yielding α'-Al$_3$(Sc$_{1-x}$Li$_x$)(L1$_2$) precipitates [28–31]. Additionally, Li provides solid-solution strengthening [32,33], while reducing the density [34,35]. Further strengthening may be achieved through precipitation of δ'-Al$_3$Li(L1$_2$) [32,33,36–46], which also results in an increase

* Corresponding author. Tel.: +1 847 491 5370; fax: +1 847 461 6573.
E-mail addresses: dunand@northwestern.edu (D.C. Dunand), matthew.krug@ge.com (M.E. Krug).
[1] Currently at: General Electric Aviation, M/D M89, One Neumann Way, Cincinnati, OH 45215, USA.

in stiffness [47–49]. Additions of Li to Al–Sc alloys have been previously studied [29,30,47–50]. In Ref. [31], Al–2.9 Li–0.11 Sc and Al–5.53 Li–0.048 Sc–0.009 Yb were aged at 325 °C. Compared to the Li-free control alloys, the alloys with Li additions exhibited increases in ambient temperature strength at peak-aging time due to: an increase in the volume fraction, φ, a decrease in the mean radius, $\langle R \rangle$, and an increase in the number density, N_V, of precipitates. A similar result was reported on related alloys in Ref. [51]; in both of these studies, Li additions also increase the time to the onset of overaging [31,51].

In the present research, we report on the effects of Li additions on the creep response at 300 °C of three alloys studied in Ref. [31]: Al–0.12 Sc, Al–2.9 Li–0.11 Sc, and Al–5.53 Li–0.048 Sc–0.009 Yb. The results are interpreted in the context of creep threshold stresses as reported for all Al–Sc–X alloys studied to date in our research group.

2. Experimental procedures

2.1. Alloy fabrication

Two Li-containing alloys, Al–2.9 Li–0.11 Sc (Al–0.76 Li–0.18 Sc, in wt.%) and Al–5.53 Li–0.048 Sc–0.009 Yb (Al–1.48 Li–0.083 Sc–0.06 Yb, in wt.%) – hereafter denoted Al–Li–Sc and Al–Li–Sc–Yb – were created by melting 99.999% pure Al, 99.9% pure Li, and Al–0.2 Sc and Al–3.7 Yb master alloys in an induction furnace at 800 °C under an overpressure of 3 atm of Ar. The melt was cast into a SiC crucible, resulting in ingots measuring ∼4.5 cm in diameter and ∼17 cm in length. A third Li-free alloy with composition Al–0.12 Sc (Al–0.20 Sc, in wt.%) – hereafter denoted Al–Sc – was obtained by melting in air the same pure Al and Al–0.2 Sc alloy in a zirconia-coated alumina crucible, placed in a resistance furnace. Because the Li-containing alloys were found to contain Si (probably from the SiC crucible), Si was intentionally added to Al–Sc, in the form of an Al–12.3 Si master alloy. The Al–Sc melt was stirred manually before casting into a graphite mold placed on an ice-cooled copper platen. The Al–Sc casting consisted of four cylinders ∼1 cm in diameter and ∼10 cm in height. Alloy compositions were verified using direct coupled plasma mass spectrometry (ATI Wah Chang) and are reported in Table 1.

To eliminate shrinkage porosity, sections of the cast materials were hot-isostatically pressed (HIPed) without cladding by Ultraclad Corp. (Andover, MA) at 516 °C for 2 h under a pressure of 103 MPa. Those HIPed sections were homogenized at 640 °C for 24 h in an atmosphere of flowing Ar, and quenched into ambient temperature water. Cylinders measuring 9 mm in diameter and several centimeters in length were removed from the HIPed sections by electrical discharge machining. The diameter of the resultant cylinders was reduced to 8 mm by machining with a lathe, and then cut to 16 mm length segments to produce compression creep specimens whose loading surfaces were parallel to within 10–20 μm. The density of a machined specimen from each alloy was measured using Archimedes' method, taking the average of five measurements (Table 2).

The machined specimens were solutionized for 20 min at 640 °C, and quenched into iced-brine at −12 °C, before isothermally aging at 325 °C to produce a fine dispersion of nanoscale α'-Al$_3$(Sc$_{1-x-y}$Li$_x$Yb$_y$)(L1$_2$) precipitates. Some alloys were

Table 1
Chemical composition of three alloys as determined by directly coupled plasma mass-spectroscopy.

Alloy	Li (at.%)	Sc (at. ppm)	Si (at. ppm)	Yb (at. ppm)
Al–Sc	–	1240 ± 30	130 ± 10	–
Al–Li–Sc	2.9 ± 0.1	1060 ± 73	180 ± 11	–
Al–Li–Sc–Yb	5.53 ± 0.05	480 ± 10	116 ± 5	92 ± 2

Table 2
Alloy densities as determined by Archimedes' method.

Alloy	Measured density, ρ_{meas} (g/cm^3)	Calculated density, ρ_{calc} (g/cm^3)	Difference, $\Delta \rho$ (%)
Al–Sc	2.705 ± 0.003	2.701	0.163
Al–Li–Sc	2.6454 ± 0.0002	2.6464	−0.035
Al–Li–Sc–Yb	2.5872 ± 0.0004	2.5940	−0.260

subsequently isochronally aged in increments of 25 °C for 1 h each, to either 425 °C or 450 °C. All aging treatments were terminated by quenching into iced brine at −12 °C. A detailed study of the microstructures produced by isothermal aging at 325 °C is given in Ref. [31].

2.2. Creep experiments

The creep specimens were placed between two boron nitride-lubricated alumina platens and subjected to uniaxial compression by two superalloy rams within a compression creep frame using constant dead loads. A split three-zone furnace heated the specimens to 300 ± 1 °C, as verified by a thermocouple placed within 1 cm of the specimen. This temperature was selected because it represents an upper limit on the temperature for creep resistance in Al–Sc-based alloys [1–5], and to facilitate comparison with our past studies on comparable alloys [9,10,17,18,20–25]. Displacements rates were monitored by measuring the position of the top compression ram with a linear variable displacement transducer, with a resolution of 6 μm, resulting in a minimum measurable strain increment of 4×10^{-4}. A typical strain vs. time plot is shown in Fig. 1 for Al–Li–Sc–Yb aged isothermally at 325 °C for 2 h, then isochronally aged to 450 °C. When a minimum displacement rate was achieved for a suitable duration, the applied load was increased. The maximum strain of a specimen at the conclusion of a test did not exceed 10%. Strain rates for a given load are determined by measuring the slope of a strain vs. time plot, in the secondary-creep regime, as indicated in Fig. 1.

2.3. Microstructure examination

Homogenized and quenched specimens were ground and polished to a 1 μm finish. Polished specimens were etched for 40 s using Keller's reagent to reveal the grain structure.
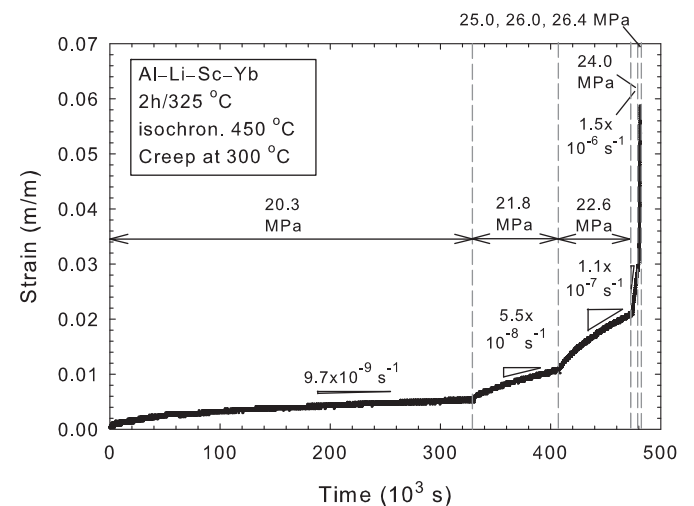

Fig. 1. Plot of compressive strain vs. time at 300 °C for several applied compressive stresses, on Al–Li–Sc–Yb alloy peak-aged isothermally for 2 h at 325 °C, and then isochronally to 450 °C.

Aged alloys were imaged using a JEOL 2100F transmission electron microscope (TEM) operated at 200 kV. Wafers ~150 μm thick were cut with a diamond saw. These were thinned to electron transparency using a Struers Tenupol 5 twin-jet electropolisher, with a one-part nitric acid to two-parts methanol electrolyte that was cooled to −35 °C using methanol and dry ice. Polishing occurred at 20 V_{dc} and ~110 mA.

Prismatic samples measuring ~$0.4 \times 0.4 \times 10\,mm^3$ were cut from the crept specimens using a low-speed diamond saw for analysis by local-electrode atom-probe (LEAP) tomography. They were then electropolished to an atomically sharp point using an electrolyte consisting of 10% perchloric acid in acetic acid at 8–24 Vdc, followed by a final polish in 2% perchloric acid in butoxyethanol. LEAP tomographic experiments were performed at specimen temperatures of $35 \pm 1\,K$ using a Cameca (formerly Imago Scientific Instruments) 4000-X Si tomograph, employing picosecond pulses of ultraviolet (355 nm) laser light at 0.075 nJ $pulse^{-1}$ at a pulse repetition rate of 500 kHz, with the specimen maintained at steady-state voltages between 3.5 and 9 kV. LEAP tomographic data were reconstructed into 3-D volumes and analyzed using IVAS version 3.4.1 software (Cameca, Madison, WI). Distances along the z-axis (parallel to the tip axis) in the datasets were calibrated by measuring the interplanar distances along low-index poles, while distances in the x- and y-dimensions were calibrated by ensuring that, after correcting for a detector efficiency of 55%, the atomic density of the reconstruction matches the literature value for pure Al, $6.02 \times 10^{28}\,m^{-3}$ [52]. For all reconstructions, these two calibrations agreed to within 5%.

To determine the precipitate radii and volume fractions from the reconstructed data, precipitates were isolated from the matrix using a modified envelope method [53], and the volume of each precipitate was recorded. The precipitate radii are determined by approximating them as volume-equivalent spheres, and the volume fraction is calculated by dividing the number of atoms in the precipitates by the total number of atoms in the reconstruction.

3. Results

3.1. Alloy chemical composition and microstructure

Compositions of the three alloys are reported in Table 1. The concentrations of Sc and Si are similar in Al–Sc and in Al–Li–Sc, permitting a direct comparison to ascertain the effects of a 2.9 at.% Li addition.

The densities of three creep specimens, one from each alloy, are shown in Table 2, along with density values calculated from lattice parameter data [35], adjusted to room temperature [7]. The measured values are in agreement with the calculated ones to within 0.3%. The addition of 2.9 and 5.53 at.% Li decreases the density of the alloys by 2.2 and 4.4%, respectively.

Fig. 2 shows an optical micrograph of the homogenized Al–Li–Sc–Yb alloy, which reveals millimeter-diameter grains, as anticipated for a cast and homogenized alloy. Fig. 2 is also typical of Al–Li–Sc and Al–Sc, which have a similar grain diameter.

Fig. 3 is a two-beam bright-field TEM image (1 1 0 zone axis, $\bar{1}$ 1 1 reflection strongly excited) of Al–Li–Sc, aged isothermally for 8 h at 325 °C and then isochronally aged to 450 °C. This aging treatment resulted in precipitates with the largest mean radius of any alloy studied in the present research, 12.3 ± 2.2 nm (Table 4). The precipitates, Fig. 3, exhibit Ashby–Brown type contrast, indicative of elastic strain in the matrix, and therefore of coherency [54]. Several isolated dislocations are also visible as lines of oscillating contrast (blue arrows), but no dislocations are found at the matrix/precipitate interfaces. The alloys therefore contain coarse
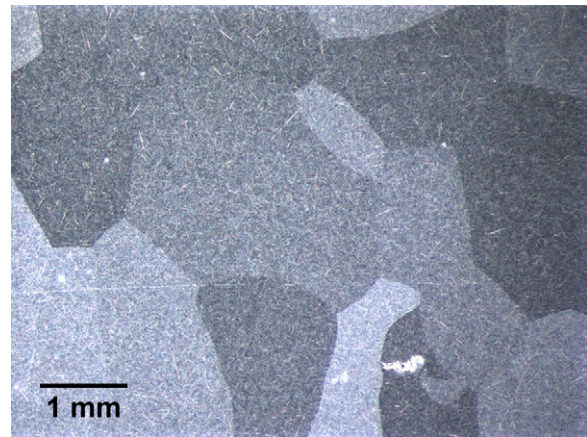

Fig. 2. Etched micrograph of a cross-section of homogenized Al–Li–Sc–Yb alloy showing coarse, millimeter-diameter grains.

grains and nanoscale coherent precipitates, two important criteria for achieving creep resistance [55].

3.2. Precipitate compositions and interfacial segregation

The composition and structure of precipitates were characterized quantitatively using the proximity histogram (or proxigram) method [56]. Fig. 4 displays plots of the proxigrams for three states: (i) isothermally peak-aged for 8 and 2 h at 325 °C for Al–Li–Sc and Al–Li–Sc–Yb, respectively; (ii) peak aged at 325 °C, isochronally aged to 425 °C, then creep tested at 300 °C; and (iii) peak-aged at 325 °C, isochronally aged to 450 °C, then creep tested at 300 °C. Fig. 4(a) and (c) also has insets that display LEAP tomographic reconstructions of a typical peak-aged precipitate.

In both alloys, after aging to 425 and 450 °C and creep testing at 300 °C, a significant Li interfacial excess develops at the α-Al matrix/α′-Al₃(Sc,Li,Yb) interface. For multi-component alloys, the excess is quantifiable using the Gibbsian adsorption isotherm [57–61]. The interfacial excess of Li relative to Al and Sc (hereafter referred to simply as the interfacial excess of Li, for brevity) is given
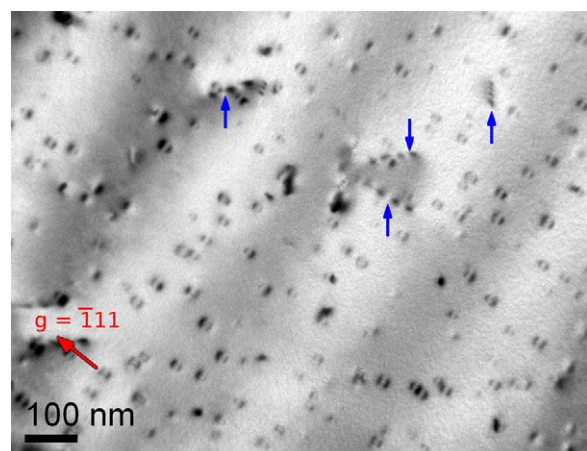

Fig. 3. TEM micrograph showing α′-Al₃(Sc,Li)(L1₂) precipitates in Al–Li–Sc aged isothermally 2 h at 325 °C and then isochronally to 450 °C. Strain-field contrast is indicative of precipitate coherency with the α-Al(f.c.c.) matrix. Dislocations in the matrix with oscillating contrast are marked with blue arrows. (For interpretation of the references to color in this figure legend, the reader is referred to the web version of the article.)
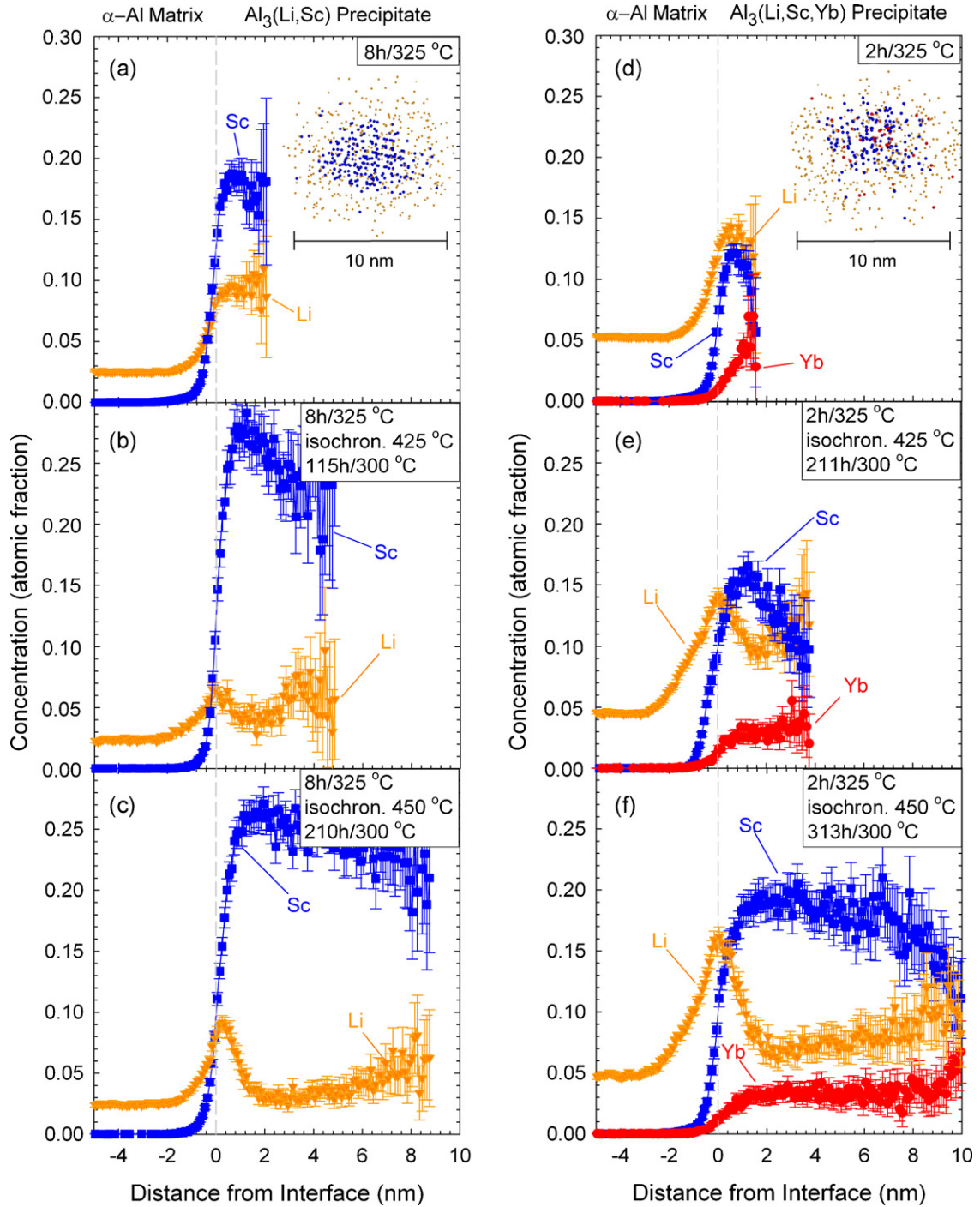
Fig. 4. Proximity histograms of precipitate compositions in (a–c) Al–Li–Sc and (d–f) Al–Li–Sc–Yb, peak-aged isothermally for 8 h (Al–Li–Sc) or for 2 h (Al–Li–Sc–Yb) at 325 °C (a and d), and further aged isochronally to 425 °C (b and e) and 450 °C (c and f). Insets in the top-right corners of (a) and (c) display LEAP tomographic reconstructions of a representative peak-aged precipitate, where Sc atoms are shown as blue spheres, Yb atoms as red spheres, and Li atoms as smaller orange points. All the Al atoms and 80% of the Li atoms are omitted for clarity. (For interpretation of the references to color in this figure legend, the reader is referred to the web version of the article.)

by [57,58]:

$$\Gamma_{Li}^{Al-Sc} = \Gamma_{Li} - \Gamma_{Sc} \frac{c_{Al}^{\alpha}c_{Li}^{\alpha'} - c_{Al}^{\alpha'}c_{Li}^{\alpha}}{c_{Al}^{\alpha}c_{Sc}^{\alpha'} - c_{Al}^{\alpha'}c_{Sc}^{\alpha}} - \Gamma_{Al} \frac{c_{Li}^{\alpha}c_{Sc}^{\alpha'} - c_{Li}^{\alpha'}c_{E}^{\alpha}}{c_{Al}^{\alpha}c_{Sc}^{\alpha'} - c_{Al}^{\alpha'}c_{Sc}^{\alpha}}$$

$$= -\left(\frac{\partial \sigma^{\alpha/\alpha'}}{\partial \mu_{Li}}\right)_{T,P,\mu_{Al},\mu_{Sc}}; \quad (1)$$

where the c_i^j are the concentrations of component i in phase j (α-Al matrix or α'-Al$_3$(Sc,Li,Yb)(L1$_2$) precipitate) $\sigma^{\alpha/\alpha'}$ is the free energy

of the α-Al/α'-Al$_3$(Sc,Li,Yb)(L1$_2$) interface, and μ_{Li} is the chemical potential of Li. The Gibbsian excess concentration of the ith component, Γ_i, is determined from the proxigram analysis, and is given by [59]:

$$\Gamma_i = \rho \Delta x \sum_{m=1}^{p} (c_i^m - c_i^k); \quad (2)$$

where ρ is the atomic density, Δx is the bin size, or distance between p layers in the proxigram, and c_i^k is the concentration
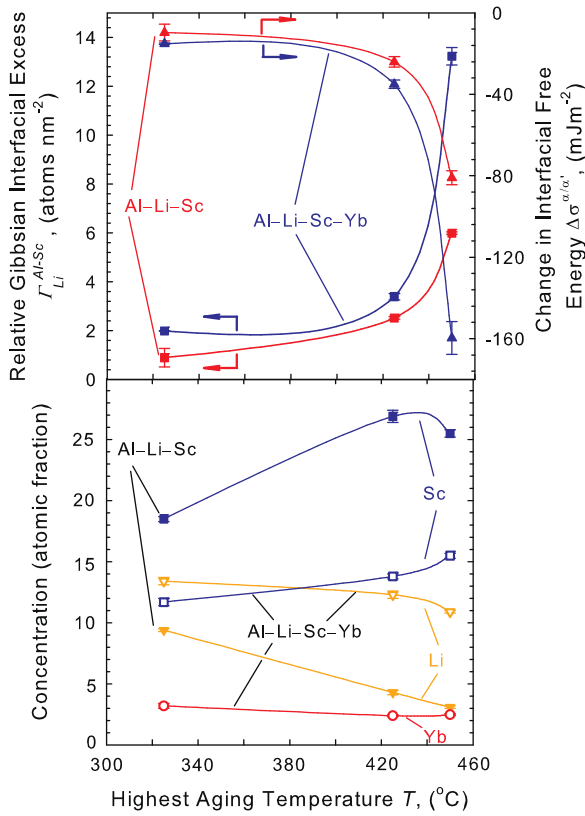
Fig. 5. Plots showing dependence upon highest aging temperature for Al–Li–Sc and Al–Li–Sc–Yb of: (a) relative interfacial excesses of Li, with respect to Al and Sc, at the matrix/precipitate interface, and the calculated resulting change in interfacial free energy; (b) solute concentrations in the precipitates, as determined by LEAP tomographic analyses.

of component i in phase k. The superscript k indicates the phase in which the proxigram is considered for each of its data points (either α or α'). A positive relative interfacial excess corresponds to a decrease in the interfacial free energy, $\Delta\sigma^{\alpha/\alpha'}$. From Eq. (1), and applying Henry's law, the change in interfacial free energy due to Li segregation at the α-Al matrix/α'-Al$_3$(Sc,Li,Yb) interface is given by

$$\Delta\sigma^{\alpha/\alpha'} = -\Gamma_{Li}^{Al-Sc}k_BT \ln\left(\frac{c_{Li}^{\alpha/\alpha',\max}}{c_{Li}^{\alpha}}\right). \tag{3}$$

where the limits of integration over the concentration of Li are taken to be $c_{Li}^{\alpha/\alpha',\max}$, the maximum concentration of Li at the α-Al matrix/α'-Al$_3$(Sc,Li,Yb) interface, and c_{Li}^{α}, the far-field concentration of Li in the α-Al matrix. Precipitate compositions, Li interfacial excesses, and the concomitant decrease in interfacial free energy are plotted as a function of the highest aging temperature in Fig. 5, and listed in Table 3. In Fig. 5(b), the precipitate compositions were calculated by excluding the Li interfacial excess. With increasing maximum aging temperature (and hence precipitate radius – Table 4, Section 3.3) there is a general trend of increasing Sc concentration, and decreasing Li and Yb concentrations in the precipitates. With increasing maximum aging temperature, the interfacial excess of Li increases for both alloys.

3.3. Creep

Fig. 6 shows the minimum compressive strain rate vs. applied uniaxial stress for the three alloys tested. The aging conditions, precipitate radii (Appendix A), and creep threshold stresses are given in
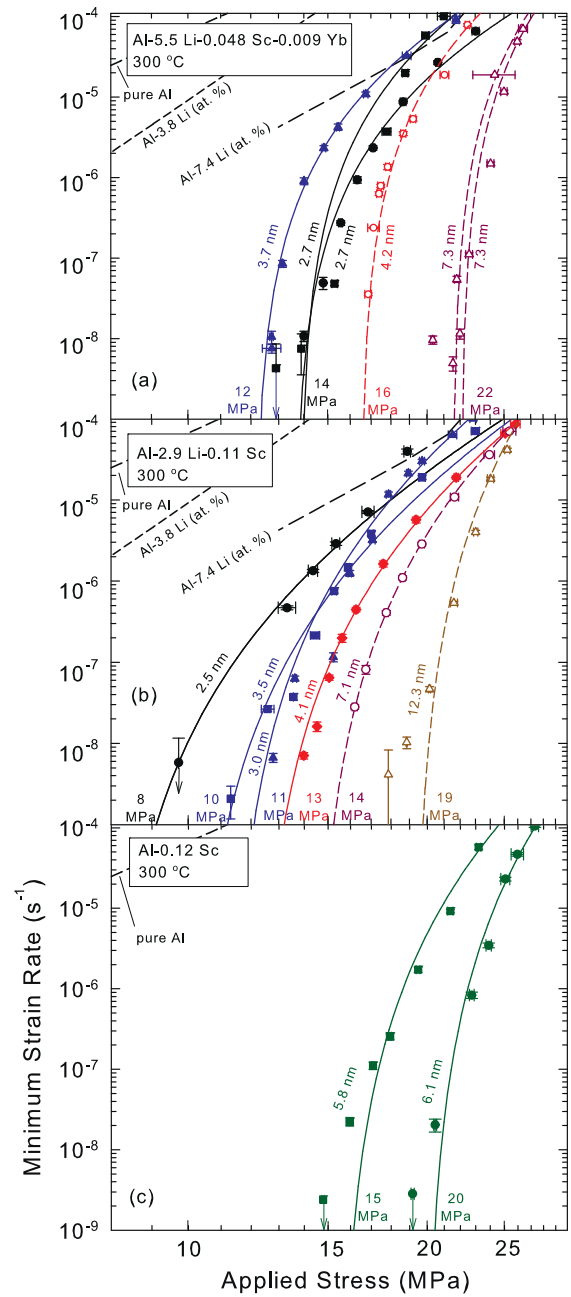

Fig. 6. Plots of minimum strain rate vs. applied stress for: (a) Al–Li–Sc–Yb; (b) Al–Li–Sc; and (c) Al–Sc alloys aged to achieve various precipitate radii (given next to curves), crept at 300 °C. Best fit lines to Eq. (4) are shown, together with resulting threshold stresses. Creep rates are also plotted for pure Al [67], Al–3.8 Li, Al–7.4 Li (at.%) [62].

Table 4. The alloys exhibit threshold stress behavior, characterized by a high apparent stress exponent, n_{ap} (between 14 and 84), similar to other Al–Sc–X alloys studied previously [9,10,17,18,20–25]. Therefore, the creep data are analyzed using a modified version of the Mukherjee–Bird–Dorn power law equation [63]:

$$\dot{\varepsilon} = A(\sigma - \sigma_{th})^n; \tag{4}$$

where A is a constant for a given temperature, σ is the applied stress, σ_{th} is the threshold stress, n is the stress exponent [64]. The threshold stress is calculated by employing a weighted linear least-squares regression of $\sqrt[n]{\dot{\varepsilon}}$ vs. σ, solving for the parameters A and σ_{th} [64]. The weight applied to the data is $1/\sigma_{\sqrt[n]{\dot{\varepsilon}}}^2$, where $\sigma_{\sqrt[n]{\dot{\varepsilon}}}$ is the uncertainty in the nth root of the strain rate. This procedure

Table 3
Solute concentrations, $c_i^{\alpha'}$, in α'-Al$_3$(Li,Sc) and α'-Al$_3$(Li,Sc,Yb) precipitates as measured by LEAP tomography, and the calculated relative interfacial excess of Li with respect to Al and Sc, Γ_{Li}^{Al-Sc}.

Alloy	Aging treatment	$c_{Li}^{\alpha'}$ (at.%)	$c_{Sc}^{\alpha'}$ (at.%)	$c_{Yb}^{\alpha'}$ (at.%)	Γ_{Li}^{Al-Sc} (atoms nm^{-2})	$\Delta\sigma^{\alpha/\alpha'}$ (mJ m^{-2})
Al–Li–Sc	8 h/325 °C	9.4 ± 0.1	18.5 ± 0.2	–	1.0 ± 0.4	−10 ± 4
	8 h/325 °C + isochronal to 425 °C	4.3 ± 0.2	26.9 ± 0.5	–	2.51 ± 0.05	−24 ± 3
	8 h/325 °C + isochronal to 450 °C	3.1 ± 0.1	25.5 ± 0.3	–	5.99 ± 0.05	−81 ± 3
Al–Li–Sc–Yb	2 h/325 °C	13.4 ± 0.3	11.7 ± 0.3	3.2 ± 0.2	1.98 ± 0.02	−15.2 ± 0.4
	2 h/325 °C + isochronal to 425 °C	12.3 ± 0.3	13.8 ± 0.2	2.4 ± 0.1	3.4 ± 0.1	−35 ± 2
	2 h/325 °C + isochronal to 450 °C	10.9 ± 0.1	15.5 ± 0.2	2.48 ± 0.08	13.2 ± 0.4	−60 ± 8

Table 4
Results of creep testing of the three alloys.

Alloy	Aging treatment	Creep time at 300 °C (h), t_{300}	Average precipitate radius (nm), $\langle R \rangle$	Threshold stress (MPa), σ_{th}	Orowan stress[a] (MPa), σ_{Or}^c	Normalized threshold stress, $\sigma_{th}/\sigma_{Or}^c$
Al–Sc	8 h/325 °C	241	6.1 ± 0.5[b]	19.9 ± 3.4	80 ± 7	0.25 ± 0.05
	24 h/325 °C	170	5.8 ± 0.5[b]	15.5 ± 2.0	83 ± 7	0.19 ± 0.03
Al–Li–Sc	24 h/325 °C	49	2.5 ± 0.1[b]	7.9 ± 0.4	166 ± 8	0.048 ± 0.003
	24 h/325 °C	426	3.0 ± 0.1	11.3 ± 0.3	150 ± 6	0.075 ± 0.004
	192 h/325 °C	75	3.5 ± 0.1[b]	10.1 ± 1.1	134 ± 6	0.075 ± 0.009
	280 h/325 °C	310	4.1 ± 0.2[b]	12.8 ± 1.1	121 ± 6	0.11 ± 0.01
	8 h/325 °C + isochronal to 425 °C	115	7.1 ± 1.1	14.4 ± 0.1	82 ± 14	0.18 ± 0.03
	8 h/325 °C + isochronal to 450 °C	210	12.3 ± 2.2	18.6 ± 2.5	54 ± 11	0.34 ± 0.08
Al–Li–Sc–Yb	2 h/325 °C	172	2.7 ± 0.2[b]	13.6 ± 1.3	147 ± 13	0.09 ± 0.01
	2 h/325 °C	190	2.7 ± 0.2[b]	13.8 ± 2.7	146 ± 13	0.09 ± 0.02
	24 h/325 °C	306	3.7 ± 0.1[b]	12.1 ± 0.8	119 ± 4	0.102 ± 0.008
	2 h/325 °C + isochronal to 425 °C	211	4.2 ± 0.2	16.5 ± 1.3	111 ± 7	0.15 ± 0.02
	2 h/325 °C + isochronal to 450 °C	313	7.3 ± 1.0	21.6 ± 7.1	74 ± 12	0.29 ± 0.11
	2 h/325 °C + isochronal to 450 °C	132	7.3 ± 1.0[b]	22.0 ± 5.0	68 ± 11	0.30 ± 0.08

[a] Calculated from Eq. (5).
[b] Estimated according to Eq. (A2).

reduces the influence of data for which the strain rate uncertainty is large [65]. Because solute atoms interact with mobile dislocations, the stress exponent, n, varies depending on the Li concentration in the alloys and the applied stress. At low stresses and high Li concentrations, solid-solution Al–Li alloys without precipitates exhibit alloy-type behavior, and have a stress exponent of about 3 [66]; whereas at high stresses and small Li concentrations, the alloys exhibit pure metal-type, or dislocation climb controlled behavior, which for pure Al is characterized by a stress exponent of 4.4 [67]. The transition stress below which $n = 3$ applies (rather than 4.4) is predicted to be 21 MPa for an Al–5.31 Li alloy and 10 MPa for an Al–2.51 Li alloy [68]. Almost all of the stresses applied to the Al–Li–Sc specimens exceed 10 MPa, and most of the stresses applied to Al–Li–Sc–Yb are under 21 MPa. Hence, in analyzing the creep data, stress exponents of 4.4 and 3 are used for Al–Li–Sc and Al–Li–Sc–Yb, respectively. For both alloys, compared to the alternative stress exponent selection, this choice also provided better linear fits to plots of $\sqrt[n]{\dot{\varepsilon}}$ vs. σ. Al–Sc is analyzed using $n = 4.4$, since the matrix is nearly pure aluminum. For all creep tests, as the applied stress increases from the threshold stress, the strain rate increases rapidly, and at greater stresses the creep rates become similar to those of precipitate-free Al and Al–Li alloys. For all three alloys, there is a general trend of increasing threshold stress (and thus creep resistance) with increasing precipitate mean radius. To remove the effect of the range of volume fractions in the various alloys, isolating the effect of the precipitates themselves, the threshold stress normalized to the calculated Orowan stress was calculated at 300 °C as [69]:

$$\sigma_{Or}^c = M \frac{0.4}{\pi} \frac{\mu b}{\sqrt{1-\nu}} \frac{\ln(2\bar{R}/b)}{\langle \lambda_{e-e}^{2D} \rangle}; \qquad (5)$$

where $M = 3.06$ is the mean Taylor matrix orientation factor [70], μ is the shear modulus of the matrix at 300 °C, b is the Burgers vector, ν is the Poisson's ratio of the matrix, $\bar{R} = 0.822\langle R \rangle$ is the

Table 5
Physical properties of the crept alloys, used in Eq. (5) and Table 4.

Property		Ref.
Mean Taylor matrix orientation factor	3.06	[70]
Burgers vector (nm)		
Al, Al–2.9 Li (at.%), Al–5.53 Li (at.%)	0.286	[35,67]
Shear modulus (GPa)		
Al	21.7	[67]
Al–2.9 Li (at.%)	23.0	[67,71]
Al–5.53 Li (at.%)	24.1	[67,71]
Poisson's ratio		
Al	0.343	[70]
Al–2.9 Li (at.%)	0.333	[70,71]
Al–5.53 Li (at.%)	0.325	[70,71]
Precipitate volume fraction (%)		
Al–0.12 Sc (at.%)	0.430 ± 0.003	[31]
Al–2.9 Li–0.11 Sc (at.%)	0.506 ± 0.007	[31], present study
Al–5.53 Li–0.048 Sc–0.009 Yb (at.%)	0.401 ± 0.001	[31], present study

mean radius for the cross-section of precipitates bisected by the glide plane for an LSW distribution of precipitates of mean radius $\langle R \rangle$, and $\langle \lambda_{e-e}^{2D} \rangle = \langle R \rangle (1.538\phi^{-1/2} - 1.643)$ is the mean edge-to-edge precipitate spacing on a glide plane, for an LSW distribution of precipitates of volume fraction φ, and mean radius $\langle R \rangle$ arranged on a square lattice [69]. Values for these parameters are given in Table 5, and the resultant normalized threshold stresses are listed in Table 4. A plot of normalized threshold stress vs. mean radius is shown for the three alloys in Fig. 7, and it exhibits a nearly linear relationship.

4. Discussion

4.1. Precipitate characteristics

In agreement with models that attribute creep resistance to lattice strains in the matrix [15,16], the creep resistance of Al–0.06 Sc–0.02 Yb and Al–0.06 Sc–0.02 Gd alloys decreases significantly
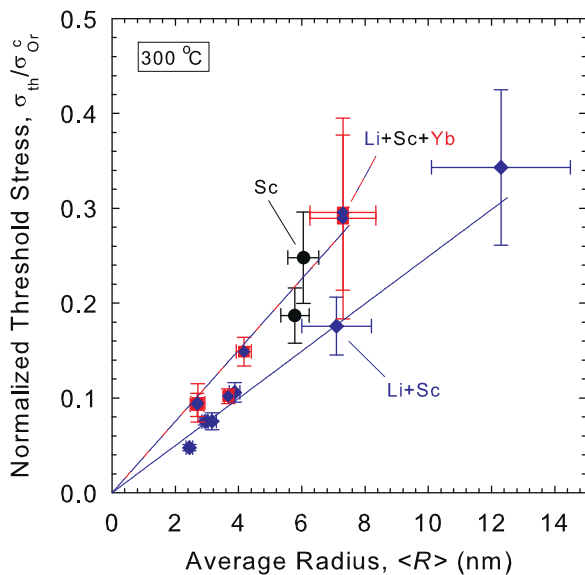
Fig. 7. Plot of threshold stresses at 300 °C, normalized to the Orowan stress, vs. average precipitate radius, ⟨R⟩. Best-fit lines to Al–Li–Sc data, and to Al–Li–Sc–Yb and Al–Sc data combined, passing through the origin, are an aid to the eye.

when strengthening precipitates lose coherency at radii approaching ~20 nm [18]. As demonstrated in Fig. 3, the lattice-mismatching precipitates that strengthen the alloys in the present research remain coherent, even for the largest precipitate mean radius, 12.3 ± 2.2 nm, in Al–Li–Sc isochronally aged to 450 °C.

As shown in Figs. 4 and 5, as the maximum aging temperature of Al–Li–Sc and Al–Li–Sc–Yb increases from 325 to 450 °C, the Li concentration of the precipitates decreases, and the excess of Li segregated at the α-Al matrix/α'-Al$_3$(Sc,Li,Yb) precipitate interface increases. After aging to 450 °C, followed by creep at 300 °C, the interfacial excess of Li increases to 5.99 ± 0.05 atoms nm^{-2} in Al–Li–Sc and to 13.2 ± 0.4 atoms nm^{-2} in Al–Li–Sc–Yb. This trend is unanticipated as the equilibrium degree of segregation for an atom that binds to the interface with a free energy ΔF, is expected to obey a Boltzmann factor, exp($\Delta F/k_B T$) [72], which decreases with increasing temperature. The system is therefore not in thermodynamic equilibrium. According to Eq. (3), this leads to changes in the matrix/precipitate interfacial free energy of -81 ± 3 and -160 ± 8 mJ m^{-2} for Al–Li–Sc and Al–Li–Sc–Yb, respectively at the maximum aging temperature of 450 °C, which are large values. For reference, the interfacial free energy of α-Al matrix/α'-Al$_3$Sc precipitates in binary Al–Sc alloys has been reported to be in the range 20–300 mJ m^{-2}, with 100–300 mJ m^{-2} being typical [73–78]. These results demonstrate that aging treatments that produce coarser precipitates lead to a greater degree of Li segregation at the α-Al matrix/α'-Al$_3$(Sc,Li,Yb) precipitate interface. Also, a decrease in the Li concentration of the precipitates is observed during precipitate coarsening (Fig. 5(b)).

Several explanations for these effects are possible: (i) the rate of Li transfer from the matrix into the precipitate during coarsening is limited by the rate of incorporation into the interface (as opposed to diffusion-limited coarsening); (ii) segregation at the interface is a lower energy state for Li atoms, relative to their partitioning into the precipitate interior (i.e. Li segregation is thermodynamically stable); or (iii) it is possible that both (i) and (ii) are responsible for the large interfacial excesses of Li. In any case, segregation of Li is anticipated to reduce the coarsening rate of the precipitates, due either to interface-limited coarsening or to a reduction in the interfacial free-energy, which drives coarsening.

Indeed, precipitate radii in Al–Li–Sc aged isothermally at 325 °C [31] increase with a time exponent of 0.192 ± 0.005, compared to

Al–0.18 Sc (at.%) aged isothermally at 300 °C [2], whose precipitates coarsened more rapidly despite the lower aging temperature, with a time exponent of 0.23 ± 0.01 (Table A1 and Figs. A1 and A2). Additional possibilities exist for the decreased rate of coarsening with Li addition. For example, interactions may be occurring among solute elements in the matrix as was suggested in a study of an Al–6.5 Li–0.07 Sc–0.02 Yb alloy [51], or between solute elements and vacancies, which changes the inter-diffusivities that govern coarsening. This was suggested in several studies in which the introduction of Sc was shown to decrease the rate of coarsening of δ'-Al$_3$Li (L1$_2$) precipitates [48–50]. Another consideration is that, depending upon the vacancy-solute binding energies, it is possible that vacancies may preferentially reside in the precipitate phase, in which case coarsening occurs through coagulation and coalescence, and smaller precipitate coarsening exponents between 1/6 and 1/5 are predicted [79].

4.2. Creep behavior

Fig. 6 shows that creep resistance in the present precipitate-strengthened alloys is significantly improved compared to pure Al or binary Al–Li. The strain rate [15] and the threshold stress [15,16] have been modeled for the case of creep controlled by dislocation-climb and bypass of lattice-mismatched precipitates. It was found that the observed normalized threshold stress values approaching unity, as are observed experimentally, can be explained by considering the effect of lattice-parameter mismatch on climbing dislocations, while models of dislocation-climb-limited creep, which neglect this effect, predict threshold stresses no larger than 5% of the Orowan stress [80–86]. In Ref. [16] the threshold stress is attributed to an attractive interaction force between precipitates and the dislocations that climbed over them. A similar pinning effect was predicted in a more sophisticated three-dimensional dislocation dynamics model of a climbing and gliding dislocation, bypassing a lattice-mismatching precipitate [87]. As shown in Fig. 7, the normalized threshold stress increases nearly linearly with mean precipitate radius for all three alloys. This trend is consistent with prior studies on Al–Sc–X alloys [9,10,17,18,20–25], and with the results of several models considering the effects of lattice-parameter-mismatched precipitates on climbing dislocations [15,16,87].

For the two largest mean precipitate radii in Al–Li–Sc, 7.1 ± 1.1 and 12.3 ± 2.2 nm (Fig. 8(a) and Table 4), it is clear that the normalized threshold stress is smaller for Al–Li–Sc than for Al–Sc alloys. As described in Section 4.3, it is anticipated that Li substitutes for Sc in α'-Al$_3$Sc(L1$_2$) precipitates, thereby reducing their lattice-parameter mismatch with the α-Al(f.c.c.) matrix. The creep resistance conferred to the alloy by those precipitates is thus degraded, relative to binary Al–Sc strengthened by α'-Al$_3$Sc(L1$_2$) precipitates, as indicated by a smaller normalized threshold stress for a given mean precipitate radius. Unlike Li, when Yb substitutes for Sc to create α'-Al$_3$(Sc$_{1-x}$Yb$_x$)(L1$_2$) precipitates, the lattice-parameter mismatch increases [14] resulting in improved creep resistance [18]. Therefore, the effects of Li and Yb substitutions of Sc in α'-Al$_3$Sc(L1$_2$) precipitates should be counteracting, as is observed (Fig. 7).

4.3. Creep behavior in other Al–Sc–X alloys

The results of all of the creep testing at 300 °C on Al–Sc–X systems published to date by our research group are collected in Fig. 8. Fig. 8(a)–(c) includes data on Al–Sc as a baseline from Refs. [9,10], and from the present study. In Fig. 8(a), Al–Sc data are plotted with Al–Li–Sc and Al–Li–Sc–Yb (present research) as well as Al–Sc–Yb data [18]. Best-fit lines, whose intercepts are forced through zero, are included for Al–Sc and Al–Li–Sc–Yb (together), Al–Li–Sc, and
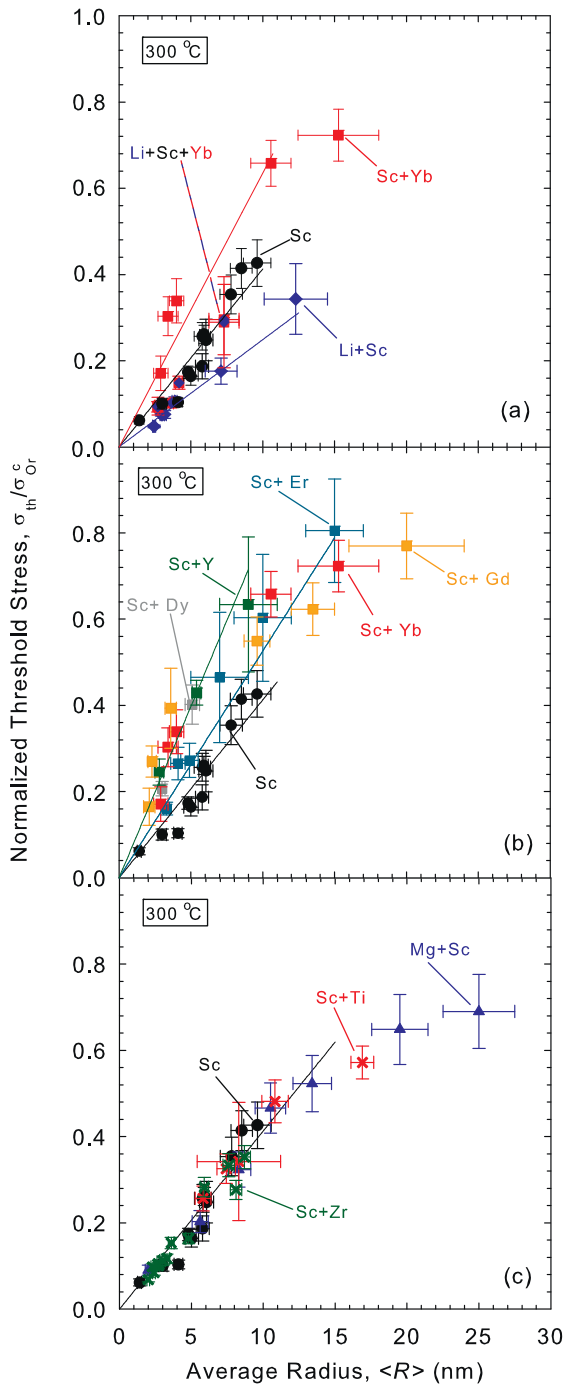
Fig. 8. Plot of threshold stresses at 300 °C normalized to the Orowan stress vs. average precipitate radius, $\langle R \rangle$, for: (a) Al–Sc and Al–Li–Sc(–Yb) [present work] and Al–Sc–Yb [18]; (b) Al–Sc–RE [17,18]; and (c) Al–Mg–Sc [25] and Al–Sc–TM alloys [20–24]. Data from prior research on binary Al–Sc alloys [9,10] are included in all plots for comparison. Best fit lines passing through the origin are shown.

Fig. 9. Plot of the slopes of linear regressions between normalized threshold stresses at 300 °C and the average precipitate radius, $\langle R \rangle$ (from Fig. 8) vs. the lattice parameter mismatch of α'-Al$_3$(Sc,X)(L1$_2$) precipitates (with measured compositions) in Al–Sc–X alloys [9,10,17,18,20–25]. (a) For each Al–Sc–X curve, the slopes are determined by a least-squares regression analysis with no constraint on their ordinate intercepts; (b) the slopes are determined similarly except that the ordinate intercepts are forced to be zero (as illustrated in Fig. 8).

passing through the origin is again shown for data with radii smaller than 13 nm for all alloys.

Linear regressions were performed on the plots of normalized threshold stress vs. mean radius, for each of the Al–Sc–X systems plotted in Fig. 8. In Fig. 9, the slopes of those regression lines are plotted as a function of the lattice-parameter mismatch of precipitates for each Al–Sc–X alloy. The lattice parameter mismatches are calculated by applying Vegard's law [88], lattice parameter data in Ref. [14], and precipitate compositions measured by LEAP tomographic analyses [12,24,26,31,89]. The lattice parameter values are then adjusted to reflect the lattice-parameter mismatch at 300 °C, thereby taking account of the effects of thermal expansion of both Al$_3$(Sc,RE)(L1$_2$) [13] and Al [7]. The change in lattice-parameter of the α-Al(f.c.c.)-matrix with Mg [26] and Li additions [35] is also taken into account. In the case of α'-Al$_3$(Sc,Li)(L1$_2$)-precipitates, the lattice parameter was calculated as described below, while for α'-Al$_3$(Li,Sc,Yb)(L1$_2$)-precipitates, the effects of Yb substitution (described above) and Li substitution (described below) are both accounted for.

No experimental measurements of the lattice parameter in the ternary α'-Al$_3$(Sc$_{1-x}$Li$_x$)(L1$_2$) phase have been made. The lattice parameter of binary δ'-Al$_3$Li(L1$_2$) is reported to be 4.01 ± 0.009 Å [90] at ambient temperature, which corresponds to an unconstrained lattice-parameter mismatch with pure Al of −0.98%. The lattice parameter of binary α'-Al$_3$Sc(L1$_2$) is 4.103 Å [6] at

Al–Sc–Yb. The last point in the Al–Sc–Yb series (mean radius of 15.3 nm) is excluded because it is considered to be an outlier as the precipitates are most likely not fully coherent at this large radius. In Fig. 8(b) data are plotted from prior studies on Al–Sc–RE alloys, where the REs include Er, Y, and Dy [17], and Yb and Gd [18]. Best-fit lines passing through the origin are plotted for Al–Sc (smallest slope), Al–Sc–Er (intermediate slope), and Al–Sc–Y (greatest slope). In Fig. 8(c), data are plotted from studies on Al–Sc–Zr [20,22], Al–Sc–Ti [23,24], and Al–Mg–Sc [25]. A best-fit line
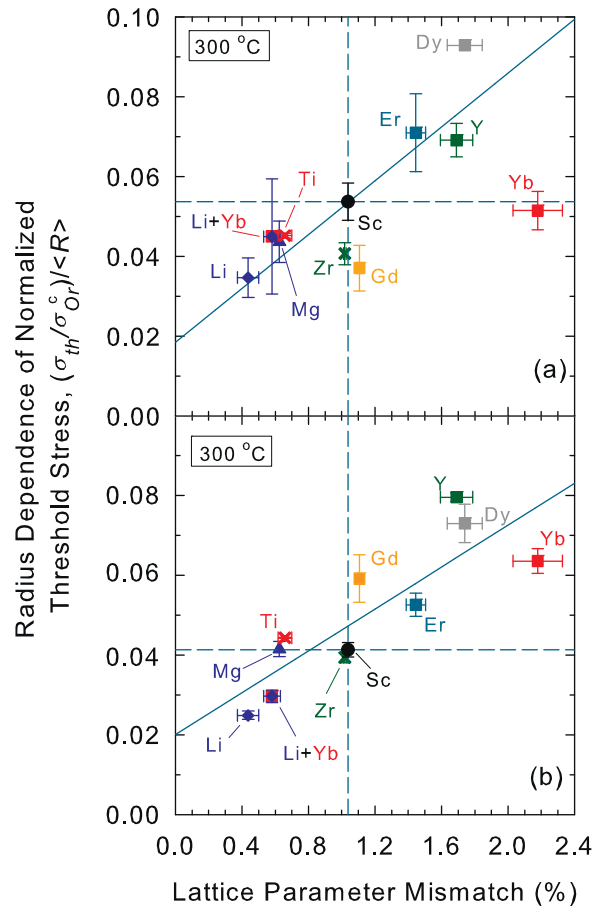
ambient temperature, corresponding to an unconstrained lattice-parameter mismatch of 1.30%. Therefore, it is anticipated that incorporation of Li into binary α'-Al$_3$Sc(L1$_2$), forming ternary α'-Al$_3$(Sc$_{1-x}$Li$_x$)(L1$_2$) results in a decrease in the lattice parameter mismatch. Confirmation of this effect was achieved using first-principles calculations to estimate the change in lattice parameter of α'-Al$_3$Sc(L1$_2$) due to Li incorporation [91]. The calculated lattice parameter of α'-Al$_{0.75}$(Sc$_{0.15}$Li$_{0.10}$)(L1$_2$), which was chosen because it is close to the experimentally measured composition of precipitates in Al–Li–Sc peak-aged 8 h at 325 °C: α'-Al$_{0.74}$(Sc$_{0.17}$Li$_{0.09}$) [31], is 4.078 Å, thereby predicting that Li incorporation into α'-Al$_3$Sc(L1$_2$) does reduce its lattice-parameter mismatch from 1.3 to 0.77% at ambient temperature, or from 1.04 and 0.51 at the creep temperature, 300 °C, assuming that the precipitates and the matrix have coefficients of thermal expansion equal to those of their Li-free counterparts [13,67].

Fig. 9 displays the relationship between an α'-Al$_3$(Sc,X)(L1$_2$) precipitate's lattice-parameter mismatch with the α-Al(f.c.c.)-matrix (calculated as described above, and using only data from mean-precipitate radii smaller than 13 nm), and its effectiveness at increasing an alloy's creep-resistance. A greater slope means that an alloy has a greater normalized threshold stress, for a given precipitate radius. In Fig. 9(a) the slopes are determined by a least-squares regression analysis with no constraint on their ordinate intercepts, while in Fig. 9(b) the ordinate intercepts are constrained to zero. Fig. 9 demonstrates a clear trend of increasing slope (and thus creep resistance) with increasing lattice-parameter mismatch. Although there is significant scatter of the data about the best-fit line, it is apparent that all the ternary additions leading to an increase in the lattice-parameter mismatch have a slope larger than that of binary Al–Sc and vice versa. Hence, the relationship between lattice-parameter mismatch of precipitates and their effectiveness at improving creep resistance, is consistent for additions of X in all Al–Sc–X studied by our research group [9,10,17,18,20–25].

In Fig. 9(a), in terms of promoting creep resistance, Dy appears to be the most effective addition to Al–Sc, while in Fig. 9(b) Y seems most effective. In Ref. [14] the lattice-parameter mismatch at ambient temperature between Al$_3$(Sc$_{1-x}$RE$_x$)(L1$_2$) and pure Al(f.c.c.) is given for each RE, where x corresponds to the maximum solubility of a RE in Al$_3$Sc(L1$_2$). At the maximum RE solubility in Al$_3$Sc(L1$_2$), the lattice-parameter mismatch of Al–Sc–Dy (3.37%) is greater than that of Al–Sc–Y (2.76%), and both are smaller than those of Al–Sc–Tm (3.46%), Al–Sc–Tb (3.50%), and Al–Sc–Ho (3.57%). The creep behavior of the latter three alloys has not yet been explored. It was shown in Ref. [12] that unlike Al–0.06 Sc–0.02 Tb and Al–0.06 Sc–0.02 Ho, Al–0.06 Sc–0.02 Tm displays a peak strength and volume fraction that compares favorably with Al–0.06 Sc–0.02 RE (at.%) alloys [12], and also exhibits an early aging response due to precipitation of Tm-rich α'-Al$_3$(Tm$_{1-x}$Sc$_x$)(L1$_2$) precipitates, similar to Al–0.06 Sc–0.02 Yb [11]. Tm is also similar to Yb in that it has full solubility in Al$_3$Sc; i.e. x in α'-Al$_3$(Tm$_{1-x}$Sc$_x$)(L1$_2$) can vary continuously from zero to one [14]. Thus, Tm is predicted to be an interesting alloying addition to improving the creep resistance of Al–Sc. Its high cost, however, makes it economically uncompetitive with Yb [19], which is relatively inexpensive among the RE elements, and imparts good creep resistance to Al–Sc (Figs. 8(b) and 9(b)).

4.4. Alloying additions to Al–Sc for use at ambient and elevated temperatures

Although Li addition improves the ambient temperature strength of binary Al–Sc alloys, Li may not be a suitable addition to Al–Sc intended for elevated temperature use. This is because its introduction degrades the creep resistance (threshold stress) of Al–Sc through a reduction in the lattice parameter mismatch of

the strengthening α'-Al$_3$(Sc,Li)(L1$_2$) precipitates. Thus, an Al–Li–Sc alloy intended for both ambient- and elevated-temperature use should also include a quaternary addition, such as Yb or other RE elements, that increases the lattice-parameter mismatch of α'-Al$_3$(Sc,Li,RE)(L1$_2$) precipitates, compensating for the deleterious effects of Li on the creep performance.

Although Li and Mg are similar alloying additions to Al–Sc as they both provide solid-solution strengthening [25,31] and reduce alloy density, they differ in several important respects. First, because Mg has no solubility in α'-Al$_3$Sc(L1$_2$) [26], it does not change significantly the lattice parameter of the precipitate, whereas Li has a high solubility in α'-Al$_3$Sc(L1$_2$), (Ref. [31], Table 3 and Fig. 5), thus decreasing its lattice parameter. The lattice parameter of the α-Al(f.c.c.)-matrix is, however, increased by dissolved Mg, and hence the α-Al(Mg)-matrix/α'-Al$_3$Sc(L1$_2$) lattice parameter mismatch is smaller in Al–Sc–Mg alloys than in binary Al–Sc [25]. For the Al–Li–Sc(–Yb) alloys studied herein the reduction in lattice-parameter mismatch with Li is greater than the effect of Mg in Ref. [25], resulting in a larger degradation in the effectiveness of the precipitates during creep (Fig. 9). Second, the coarsening rate of α'-Al$_3$Sc(L1$_2$) precipitates during isothermal aging at 300 °C is not significantly affected by the introduction of 2.2 at.% Mg [92], whereas the coarsening rate of α'-Al$_3$(Sc,Li)(L1$_2$) precipitates in Al–2.9 Li–0.11 Sc (at.%) is somewhat reduced (Figs. A1 and A2). Therefore, although the creep resistance of Al–Sc is degraded by a Li addition, the alloy resists overaging for a greater duration. By making additions of both Mg and Li to an Al–Sc alloy, it is anticipated that the lattice-parameter mismatch effects in the matrix would be counteracting, while the solid-solution strengthening effects would superimpose.

Finally, a Zr addition does not improve the creep resistance of Al–Sc alloys (Figs. 8(c) and 9). However, because Zr has a diffusivity in Al four orders of magnitude smaller than that of Sc at 300 °C [55], it dramatically improves the coarsening resistance of precipitates in Al–Sc, making them kinetically stable for longer durations and to greater temperatures [93–95]. It would therefore be of interest to explore the ambient and elevated-temperature strength in an Al–Li–Mg–Zr–Sc–Yb alloy, with the following attributes: (i) a large solid-solution strength due to Li and Mg; (ii) excellent coarsening-resistance to high temperatures due to Zr; (iii) a large lattice-parameter mismatch due to the counteracting effects of Li and Mg on the lattice parameter of the α-Al(Li,Mg)(f.c.c.) matrix, and similarly counteracting effects of Li and Yb on the lattice parameter of α'-Al$_3$(Li,Sc,Yb)(L1$_2$) precipitates; and (iv) a larger volume fraction of α'-Al$_3$(Li,Sc,Yb)(L1$_2$) precipitates as compared to α'-Al$_3$Sc(L1$_2$) precipitates in a binary Al–Sc alloy.

5. Summary and conclusions

Three cast alloys (Al–0.12 Sc, Al–2.9 Li–0.11 Sc, and Al–5.53 Li–0.048 Sc–0.009 Yb (at.%) referred to as Al–Sc, Al–Li–Sc and Al–Li–Sc–Yb, respectively) were aged isothermally at 325 °C, and in some cases additionally aged isochronally to 425 or 450 °C. The alloys were analyzed by transmission electron microscopy (TEM) and local-electrode atom-probe (LEAP) tomography, and creep tested at 300 °C, with the following results:

- The alloys contain coherent, nanosize α'-Al$_3$(Li,Sc,Yb)(L1$_2$) precipitates that induce elastic strains in the matrix, as determined by two-beam TEM imaging. In Li-containing alloys, LEAP tomographic analyses demonstrate that, as the precipitates coarsen due to isochronal aging at increasing temperatures, their Li (and Yb) concentrations decrease and their Sc concentrations increase.
- A relative interfacial excess of Li with respect to Al and Sc develops at the matrix/precipitate interface as the

precipitates coarsen in Li-containing alloys. The excess is greatest for the largest precipitates in both alloys, after aging isochronally to 450 °C, and additional creep testing at 300 °C. The interfacial excess of Li is greater in Al–Li–Sc–Yb ($\Gamma_{\text{Li}}^{\text{Al–Sc}} = 13.2 \pm 0.4$ atoms nm^{-2}, $\langle R \rangle = 7.3 \pm 1.0$ nm) than in Al–Li–Sc ($\Gamma_{\text{Li}}^{\text{Al–Sc}} = 5.99 \pm 0.05$ atoms nm^{-2}, $\langle R \rangle = 12.3 \pm 2.2$ nm), corresponding to changes in the interfacial free energies of -160 ± 8 and -81 ± 3 mJ m^{-2}, respectively.

- The aged alloys exhibit threshold stresses during creep deformation at 300 °C, ranging from ~8 to 22 MPa. For a given alloy, the threshold stress increases with the mean precipitate radius.
- Al–Li–Sc has lower threshold stresses, at a given precipitate size, than both Al–Sc and Al–Li–Sc–Yb. This is explained by the fact that Li substitution of Sc atoms in α'-Al$_3$(Sc,Li)(L1$_2$) precipitates causes a decrease in the lattice-parameter mismatch with the α-Al matrix, reducing precipitate/dislocation elastic interactions. For α'-Al$_3$(Li,Sc,Yb)(L1$_2$) precipitates in Al–Li–Sc–Yb, Sc substitution by both Li and Yb occurs. Because Yb increases the lattice-parameter mismatch with the α-Al(f.c.c.) matrix, while Li decreases it, the effects are counteracting, and the creep resistance is the same as that of binary Al–Sc.
- Creep threshold stresses (normalized to the Orowan stress) for different dilute Al–Sc–X alloys measured previously at 300 °C, are plotted against matrix/precipitate lattice-parameter mismatch. When X is a rare-earth element, the creep resistance of the alloys increases due to an increase in the lattice-parameter mismatch. When X is Li, Mg, or a transition metal (Ti or Zr), the creep resistance of the alloys decreases due to a decrease in the lattice-parameter mismatch. These results are in agreement with the predictions of models that attribute the threshold stress to elastic interactions between coherent precipitates with size- and shear modulus-mismatch with the matrix, and dislocations that bypass them by a climb mechanism.

Acknowledgments

Appendix A. Precipitate radius evolution

LEAP tomographic analysis of the crept specimens was used to measure precipitate radii in several cases, but it was impractical to conduct LEAP tomographic experiments on all fourteen creep specimens. Therefore, some mean precipitate radii were interpolated from measured ones, as explained below.

Kuehmann and Voorhees (KV) [96] extended the LSW binary-alloy precipitate coarsening model [97,98] for ternary alloys, for
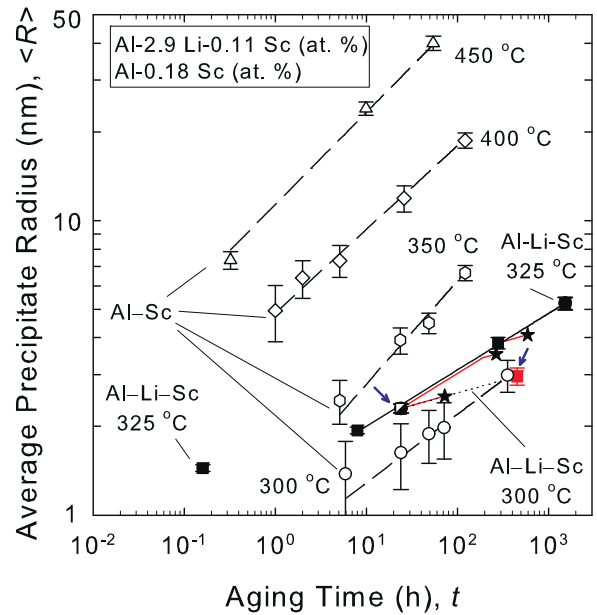

Fig. A1. Aging-time dependence of average precipitate radii, $\langle R \rangle$, for Al–0.18 Sc (at.%) aged at temperatures between 300 and 450 °C (data from [2]), and for Al–Li–Sc aged at 325 °C (data from [31]), and aged 8 h at 325 °C then crept at 300 °C for 426 h (partially filled and red squares, dotted line, indicated by blue arrows). Red lines show the assumed radius evolution of Al–Li–Sc specimens aged at 325 °C then crept at 300 °C for various durations: black stars are corresponding calculated radii (Table 4). (For interpretation of the references to color in this figure legend, the reader is referred to the web version of the article.)

which the time dependence of the mean precipitate radius is given by:

$$\langle R(t) \rangle^n - \langle R(t_0) \rangle^n = K_{\text{KV}}(t - t_0) \tag{A1}$$

where $\langle R(t) \rangle$ is the time-dependent mean precipitate radius, $\langle R(t_0) \rangle$ is the mean radius of a precipitate at a time t_0 after the onset of quasi-steady-state coarsening, K_{KV} is the coarsening rate constant, and $1/n$ is the time exponent for precipitate coarsening, which has a model value of $1/n = 1/3$. Data on precipitate coarsening in Al–Li–Sc aged at 325 °C were analyzed according to Eq. (A1), but neglecting $\langle R(t_0) \rangle$ and t_0, whose values were found to be negligibly small for all cases. Values for K_{KV} and n in Al–Li–Sc [31] and in Al–0.18 Sc, at.% (Al–0.30 Sc, wt.%) [2] are listed in Table A1, and values for n are plotted in Fig. A2.

To estimate mean precipitate radii, we further make the simplifying assumption that precipitates in a specimen aged at 325 °C coarsen according to a time exponent $1/n_{325}$, until they are crept at 300 °C, whereupon they immediately begin coarsening according to a time exponent $1/n_{300}$. Although this treatment is not based on a coarsening model, it is a pragmatic construct for predicting precipitate radii during aging and creep experiments. Mathematically, these assumptions are expressed by:

$$\langle R(t_{325}, t_{300}) \rangle = \langle R(t_m) \rangle \left(\frac{t_{325} + t_m}{t_m} \right)^{1/n_{325}} \left(\frac{t_{300} + t_{325} + t_m}{t_{325} + t_m} \right)^{1/n_{300}}; \tag{A2}$$

where $\langle R(t_{325}, t_{300}) \rangle$ is the mean precipitate radius after aging at 325 °C and subsequent creep at 300 °C, t_m is the closest aging time at which an experimental measurement was made of the mean precipitate radius, $\langle R(t_m) \rangle$, t_{325} is the additional aging time at 325 °C beyond the time t_m, and t_{300} is the time that the specimen temperature is maintained at 300 °C until measurable creep begins.

Specifically, as illustrated in Fig. A1, Al–Li–Sc aged for 24 h at 325 °C and then crept at 300 °C for 426 h follows the trajectory of the filled black-squares until it reaches the half-filled square (first

Table A1
Coarsening parameters in Eq. (A1), used for estimating precipitate radii in crept specimens in Eq. (A2).

Alloy (at.%)	Temperature (°C), T	Coarsening rate constant, K_{KV}	Time exponent, $1/n$	Ref.
Al–2.9 Li–0.11 Sc	300	–[a]	0.086	Present work
Al–2.9 Li–0.11 Sc	325	$1.1 \pm 0.2 \times 10^{-50}$	0.192 ± 0.005	[31]
Al–0.18 Sc	300	$2.0 \pm 0.4 \times 10^{-43}$	0.23 ± 0.01	[10]
Al–0.18 Sc	325	–	0.24 ± 0.01	Interpolated from data in [10]
Al–0.18 Sc	350	$1.1 \pm 0.7 \times 10^{-29}$	0.35 ± 0.04	[10]
Al–0.18 Sc	400	$1.5 \pm 0.5 \times 10^{-33}$	0.284 ± 0.009	[10]
Al–0.18 Sc	450	$1.2 \pm 0.7 \times 10^{-29}$	0.31 ± 0.02	[10]

[a] No value is reported, because the aging treatment at 300 °C follows an earlier one at 325 °C, which artificially reduces K_{KV}.

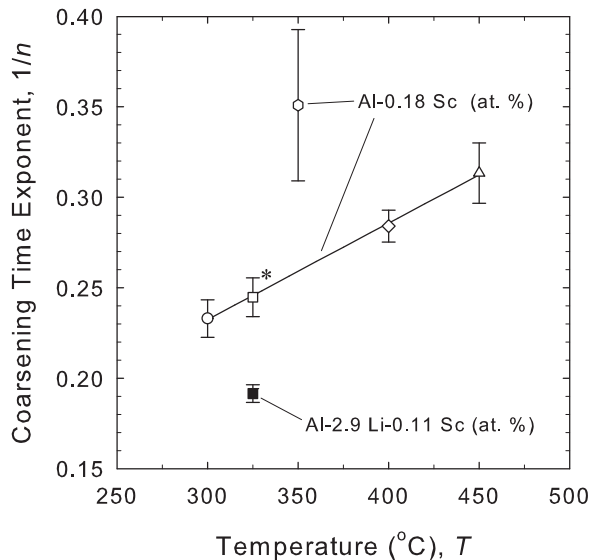**Fig. A2.** Temperature dependence of coarsening time exponent (Eq. (A1)) in Al–0.18 Sc (at.%) aged at temperatures from 300 to 450 °C [2], and in Al–0.11 Sc (at.%) aged at 325 °C [31]. The unfilled square marked by an asterisk corresponds to a value interpolated from the best-fit trend line to the data for Al–0.18 Sc (at.%), excluding the outlier at 350 °C.

arrow), where, upon reducing the temperature to 300 °C, the precipitates then follow the dotted trajectory toward the red square (second arrow). These two points represent measured precipitate radii. In Fig. A1, red lines indicate the assumed precipitate radius trajectory during creep at 300 °C, and the calculated precipitate radii reported in Table 4 are indicated by black stars. A similar approach is employed to predict mean radii in Al–Li–Sc–Yb, using the values for $1/n$ measured in Al–Li–Sc (Table A1 and Fig. A2). Precipitate radii in Al–Sc are also estimated by this approach, using values of n calculated from data on coarsening of Al–0.18 Sc [2] (Fig. A1). A value for the coarsening time exponent in Al–Sc at 325 °C is interpolated from the data in the range 300–450 °C.

References

[1] M.Y. Drits, L.B. Ber, Y.G. Bykov, L.S. Toropova, G.K. Anastas'eva, Phys. Met. Metallogr. 57 (1984) 118–126.
[2] E.A. Marquis, D.N. Seidman, Acta Mater. 49 (2001) 1909–1919.
[3] L.S. Toropova, D.G. Eskin, M.L. Kharakterova, T.B. Dobatkina, Advanced Aluminum Alloys Containing Scandium, Gordon & Breach, Amsterdam, 1998.
[4] R.W. Hyland Jr., Metall. Mater. Trans. A 23 (1992) 1947–1955.
[5] J. Røyset, N. Ryum, Int. Mater. Rev. 50 (2005) 19–44.
[6] J.L. Murray, J. Phase Equilib. 19 (1998) 380–384.
[7] J. Røyset, N. Ryum, Scripta Mater. 52 (2005) 1275–1279.
[8] C.B. Fuller, D.N. Seidman, D.C. Dunand, Scripta Mater. 40 (1999) 691–696.
[9] D.N. Seidman, E.A. Marquis, D.C. Dunand, Acta Mater. 50 (2002) 4021–4035.
[10] E.A. Marquis, D.N. Seidman, D.C. Dunand, Acta Mater. 51 (2003) 285–287.
[11] R.A. Karnesky, M.E. vanDalen, D.C. Dunand, D.N. Seidman, Scripta Mater. 55 (2006) 437–440.
[12] M.E. Krug, A. Werber, D.C. Dunand, D.N. Seidman, Acta Mater. 58 (2010) 134–145.
[13] Y. Harada, D.C. Dunand, Scripta Mater. 48 (2003) 219–222.
[14] Y. Harada, D.C. Dunand, Intermetallics 17 (2009) 17–24.
[15] E.A. Marquis, D.C. Dunand, Scripta Mater. 47 (2002) 503–508.
[16] M.E. Krug, D.C. Dunand, Acta Mater. 59 (2011) 5125–5134.
[17] R.A. Karnesky, D.N. Seidman, D.C. Dunand, Mater. Sci. Forum 519–521 (2006) 1035–1040.
[18] M.E. van Dalen, D.C. Dunand, D.N. Seidman, Acta Mater. 59 (2011) 5224–5237.
[19] A. Naumov, Russ. J. Non-Ferrous Met. 49 (2008) 14–22.
[20] C.B. Fuller, D.N. Seidman, D.C. Dunand, Acta Mater. 51 (2003) 4803–4814.
[21] K.E. Knipling, D.C. Dunand, Scripta Mater. 59 (2008) 387–390.
[22] K.E. Knipling, D.N. Seidman, D.C. Dunand, Acta Mater. 59 (2011) 943–954.
[23] M.E. van Dalen, D.C. Dunand, D.N. Seidman, Acta Mater. 53 (2005) 4225–4235.
[24] M.E. van Dalen, D.N. Seidman, D.C. Dunand, Acta Mater. 56 (2008) 4369–4377.
[25] E.A. Marquis, D.N. Seidman, D.C. Dunand, Acta Mater. 51 (2003) 4751–4760.
[26] E.A. Marquis, D.N. Seidman, M. Asta, C. Woodward, V. Ozolins, Phys. Rev. Lett. 91 (2003) 036101:1–036101:4.
[27] B. Hallstedt, O. Kim, Int. J. Mater. Res. 98 (2007) 961–969.
[28] R.A. Emigh, The aluminum–scandium–lithium–magnesium system as a potential source of superplastically formable alloys, Ph.D. Thesis, University of California, Berkeley, 1990.
[29] R.A. Emigh, E.L. Bradley, J.W. Morris, in: E.W. Lee, N.J. Kim (Eds.), Light-weight Alloys for Aerospace Applications II, TMS, 1991, pp. 27–43.
[30] M.E. Krug, D.C. Dunand, D.N. Seidman, Appl. Phys. Lett. 92 (2008) 124107.
[31] M.E. Krug, D.C. Dunand, D.N. Seidman, Acta Mater. 59 (2011) 1700–1715.
[32] S.M. Jeon, J.K. Park, Philos. Mag. A 70 (1994) 493–504.
[33] E. Nembach, Prog. Mater. Sci. 45 (2000) 275–338.
[34] W. Gasior, Z. Moser, J. Pstrus, J. Phase Equilib. Diffus. 19 (1998) 234–238.
[35] E. Levine, E. Rapperport, Trans. Metall. Soc. AIME 227 (1963) 1204–1208.
[36] S.F. Baumann, D.B. Williams, Metall. Mater. Trans. A 16 (1985) 1203–1211.
[37] S.F. Baumann, D.B. Williams, Acta Metall. Mater. 33 (1985) 1069–1078.
[38] K. Hono, S.S. Babu, K. Hiraga, R. Okano, T. Sakurai, Acta Metall. Mater. 40 (1992).
[39] U. Messerschmidt, M. Bartsch, Mater. Sci. Eng. A: Struct. Mater. Prop. Microstruct. Process. 164 (1993) 332–339.
[40] Y. Miura, A. Matsui, M. Furukawa, M. Nemoto, Aluminium–Lithium Alloys III, Institute of Metals, Oxford, England, United Kingdom, 1986, pp. 427–434.
[41] B. Noble, S.E. Bray, Philos. Mag. A: Phys. Condens. Matter Defects Mech. Prop. 79 (1999) 859–872.
[42] T.H. Sanders, E.A. Starke, Acta Metall. 30 (1982) 927–939.
[43] G. Schmitz, P. Haasen, Acta Metall. Mater. 40 (1992) 2209–2217.
[44] G. Schmitz, K. Hono, P. Haasen, Acta Metall. Mater. 42 (1994) 201–211.
[45] D.B. Williams, in: T.H.J. Sanders, E.A.J. Starke (Eds.), Aluminum–Lithium Alloys, Proceedings of the First International Aluminum–Lithium Conference, Metallurgical Society of AIME, 1981, pp. 89–100.
[46] D.B. Williams, J.W. Edington, Met. Sci. 9 (1975) 529–532.
[47] A.L. Beresina, N.I. Kolobnev, K.V. Chuistov, A.V. Kotko, O.A. Molebny, Mater. Sci. Forum 396–402 (2002) 977–982.
[48] A.L. Berezina, V.A. Volkov, C.V. Ivanov, N.I. Kolobnev, K.V. Chuistov, Fiz. Met. Metalloved. 2 (1991) 172–180.
[49] C. Joh, K. Yamada, Mater. Trans. JIM 40 (1999) 439–442.
[50] Y. Miura, K. Horikawa, K. Yamada, M. Nakayama, Aluminum Alloys: Their Physical and Mechanical Properties, 1994, pp. 161–168.
[51] C. Monachon, M.E. Krug, D.N. Seidman, D.C. Dunand, Acta Mater. 59 (2011) 3398–3409.
[52] W.B. Pearson, A Handbook of Lattice Spacings and Structures of Metals and Alloys, Pergamon Press, London, 1967.
[53] M.K. Miller, E.A. Kenik, Microsc. Microanal. 10 (2004) 336–341.
[54] M.F. Ashby, L.M. Brown, Philos. Mag. 8 (1963) 1083–1102.
[55] K.E. Knipling, D.C. Dunand, D.N. Seidman, Z. Metallkd. 97 (2006) 246–265.
[56] O.C. Hellman, J.A. Vandenbroucke, J. Rüsing, D. Isheim, D.N. Seidman, Microsc. Microanal. 6 (2000) 437–444.
[57] R. Defay, I. Prigogine, A. Bellemans, Surface Tension and Adsorption, Wiley, 1966.
[58] S.A. Dregia, P. Wynblatt, Acta Metall. Mater. 39 (1991) 771–778.
[59] O.C. Hellman, D.N. Seidman, Mater. Sci. Eng. A 327 (2002) 24–28.
[60] D. Isheim, M.S. Gagliano, M.E. Fine, D.N. Seidman, Acta Mater. 54 (2006) 841–849.
[61] A.P. Sutton, R.W. Balluffi, Interfaces in Crystalline Materials, Clarendon Press/Oxford University Press, Oxford/New York, 1995.
[62] K. Ellison, T. McNelley, A. Fox, Metall. Trans. A: Phys. Metall. Mater. Sci. 24 (1993) 2001–2007.
[63] A.K. Mukherjee, J.E. Bird, J.E. Dorn, ASTM Trans. Q. 62 (1969) 155–179.

[64] R. Lagneborg, B. Bergman, Met. Sci. 10 (1976) 20–28.
[65] R.A. Karnesky, Mechanical properties and microstructure of Al–Sc with rare-earth element or Al_2O_3 additions, Ph.D. Thesis, Northwestern University, Evanston, IL, 2007.
[66] A. Ali, M. Fahim, F. Mansy, J. Mater. Sci. Lett. 8 (1989) 841–843.
[67] H.J. Frost, M.F. Ashby, Deformation-Mechanism Maps, Pergamon Press, Oxford, 1982.
[68] J. Friedel, Dislocations, Pergamon, Oxford, 1964.
[69] E. Nembach, Particle Strengthening of Metals and Alloys, Wiley-Interscience, New York, 1996.
[70] M.A. Meyers, K.K. Chawla, Mechanical Metallurgy: Principles and Applications, Prentice-Hall, Englewood Cliffs, NJ, 1984.
[71] W. Mueller, E. Bubek, M. Gerold, Aluminium–Lithium Alloys III, Institute of Metals, Oxford, England, United Kingdom, 1985, pp. 435–441.
[72] D.A. Porter, K.E. Easterling, Phase Transformations in Metals and Alloys, Taylor & Francis, Boca Raton, 2004.
[73] M. Asta, V. Ozolins, C. Woodward, JOM 53 (2001) 16–19.
[74] S. Iwamura, Y. Miura, Acta Mater. 52 (2004) 591–600.
[75] G.M. Novotny, A.J. Ardell, Mater. Sci. Eng. A 318 (2001) 144–154.
[76] J. Røyset, N. Ryum, Mater. Sci. Eng. A 396 (2005) 409–422.
[77] C. Watanabe, T. Kondo, R. Monzen, Metall. Mater. Trans. A 35 (2004) 3003–3008.
[78] H.-H. Jo, S.-I. Fujikawa, Mater. Sci. Eng. A 171 (1993) 151–161.
[79] J.M. Roussel, P. Bellon, Phys. Rev. B 63 (2001).
[80] E. Arzt, M.F. Ashby, Scripta Metall. 16 (1982) 1285–1290.
[81] W. Blum, B. Reppich, in: R.W. Evans, B. Wilshire (Eds.), Creep Behaviour of Crystalline Solids, Ashgate Publishing, 1985, pp. 83–135.
[82] J. Cadek, Creep in Metallic Materials, Elsevier, Amsterdam, 1988, pp. 176–204.
[83] J.H. Hausselt, W.D. Nix, Acta Metall. 25 (1977) 1491–1502.
[84] R. Lagneborg, Scripta Metall. 7 (1973) 605–613.
[85] R.N. Nabarro, H.L.d. Villiers, The Physics of Creep: Creep and Creep-resistant Alloys, Taylor & Francis, London, 1995.
[86] J. Rösler, E. Arzt, Acta Metall. 36 (1988) 1043–1051.
[87] Y. Xiang, D.J. Srolovitz, Philos. Mag. 86 (2006) 3937–3957.
[88] L. Vegard, Z. Phys. A: Hadrons Nuclei 5 (1921) 17–26.
[89] C.B. Fuller, J.L. Murray, D.N. Seidman, Acta Mater. 53 (2005) 5401–5413.
[90] T. Yoshi-yama, K. Hasebe, M.-h. Mannami, J. Phys. Soc. Jpn. 25 (1968) 908.
[91] Z. Mao, personal communication, 2011.
[92] E.A. Marquis, D.N. Seidman, Acta Mater. 53 (2005) 4259–4268.
[93] V.G. Davydov, V.I. Elagin, V.V. Zakharov, T.D. Rostova, Met. Sci. Heat Treat. 38 (1996) 347–352.
[94] C.B. Fuller, D.N. Seidman, Acta Mater. 53 (2005) 5415–5428.
[95] V.I. Yelagin, V.V. Zakharov, S.G. Pavlenko, T.D. Rostova, Phys. Met. Metallogr. 60 (1985) 88–92.
[96] C.J. Kuehmann, P.W. Voorhees, Metall. Mater. Trans. A 27 (1996) 937–943.
[97] I.M. Lifshitz, V.V. Slyozov, J. Phys. Chem. Solids 19 (1961) 35–50.
[98] C. Wagner, Z. Elektrochemie 65 (1961) 581–591.